View metadata, citation and similar papers at core.ac.uk

brought to you by CORE

Crystal orientation effect on spin injection/detection efficiency in Si lateral spin-valve devices

Mizue Ishikawa,[1] Makoto Tsukahara,[1] Syuta Honda,[2,3] Yuichi Fujita,[1] Michihiro Yamada,[1] Yoshiaki Saito,[4] Takashi Kimura,[3,5] Hiroyoshi Itoh,[2,3] and Kohei Hamaya[1,3]

[1]Department of Systems Innovation, Graduate School of Engineering Science, Osaka University, 1-3 Machikaneyama, Toyonaka 560-8531, Japan.

[2]Department of Pure and Applied Physics, Faculty of Engineering Science, Kansai University, 3-3-35 Yamate, Suita 564-8680, Japan.

[3]Center for Spintronics Research Network, Graduate School of Engineering Science, Osaka University, 1-3 Machikaneyama, Toyonaka 560-8531, Japan.

[4]Center for Innovative Integrated Electronic System, Tohoku University, 468-1 Aramaki-Aza-Aoba, Sendai 980-0845, Japan

[5]Department of Physics, Kyushu University, 744 Motooka, Fukuoka 819-0395, Japan.

E-mail: `hamaya@ee.es.osaka-u.ac.jp`

17 October 2018

Abstract. We show evident crystal orientation effect on pure spin current transport in Si-based lateral spin-valve (LSV) devices with epitaxially grown CoFe/MgO tunnel contacts. When we compare nonlocal spin signals between LSV devices along $\langle 100\rangle$ (Si$\langle 100\rangle$) and $\langle 110\rangle$ (Si$\langle 110\rangle$), we find that the magnitude of the spin signals for Si$\langle 100\rangle$ LSV devices is always larger than that for Si$\langle 110\rangle$ LSV devices. The analyses based on the one-dimensional spin diffusion model reveal that the spin-diffusion length and spin lifetime between Si$\langle 100\rangle$ and Si$\langle 110\rangle$ LSV devices are comparable, while the spin injection/detection efficiency in Si$\langle 100\rangle$ LSV devices is evidently larger than that in Si$\langle 110\rangle$ ones. Possible origins of the difference in the spin injection/detection efficiency between Si$\langle 100\rangle$ and Si$\langle 110\rangle$ LSV devices are discussed.

Submitted to: *J. Phys. D: Appl. Phys.*

1. Introduction

In the field of spintronics [1–4], spin-based logic devices using semiconductors have so far been proposed theoretically [5–8]. To achieve these concepts, electrical spin injection, transport, and detection in semiconductors have been explored by using nonlocal magnetoresistance measurements in lateral spin-valve (LSV) devices with GaAs [9–15], Si [16–21], and Ge [22–28]. Although almost all the studies have used single crystalline semiconductor layers as the pure-spin-current transport channels, there has still been lack of information on the influence of the crystal orientation on the spin injection, transport, and detection in semiconductors.

To date, Li *et al.* have clarified the influence of the g-factor anisotropy in the Ge conduction band on the spin relaxation of electrons by combining a ballistic hot electron spin injection-detection technique with changing in-plane applied magnetic field directions [29]. Unfortunately, the above study did not show the pure spin current transport in the nonlocal magnetoresistance measurements. Recently, Park *et al.* reported the crystallographic-dependent pure spin current transport in GaN-based LSV devices with nanowire channels at room temperature [30]. They discussed the influence of the spontaneous polarization, interface-specific spin filtering, or the strength of the spin-orbit coupling on the pure spin current transport in GaN nanowires. However, the detailed mechanism is still an open question.

On the other hand, the crystal orientation effect on the spin injection in semiconductors has been discovered in (Ga,Mn)As/GaAs LSV devices [31]; for ferromagnetic (Ga,Mn)As contacts, there is the tunneling anisotropic spin polarization depending on the crystal orientation of GaAs. After that, using three-terminal Hanle-effect measurements, similar phenomena for various ferromagnetic metal contacts have been observed in Si [32, 33]. According to the previous works on Si [32, 33], the anisotropy of the tunneling spin polarization is attributed to the magnetization direction of ferromagnetic contacts relative to the crystal orientation of semiconductors. However, since the the pure-spin-current transport cannot be investigated by the three-terminal Hanle-effect measurements, the relationship between the crystal orientation of Si and the pure-spin-current transport in Si remains an open question.

In this article, we investigate the effect of crystal orientation on the pure-spin-current transport in Si-LSV devices with epitaxially grown CoFe/MgO tunnel contacts. When the crystal orientation of the spin-transport channel in LSV devices is changed from $\langle 110 \rangle$, which is a conventional cleavage direction, to $\langle 100 \rangle$, the magnitude of the spin signals is always enhanced at various conditions. From the analyses based on the one-dimensional spin diffusion model, we reveal that the spin-diffusion length and spin lifetime between Si$\langle 100 \rangle$ and Si$\langle 110 \rangle$ LSV devices are comparable, while the spin injection/detection efficiency in Si$\langle 100 \rangle$ LSV devices is evidently larger than that in Si$\langle 110 \rangle$ ones. Possible origins of the difference in the spin injection/detection efficiency between Si$\langle 100 \rangle$ and Si$\langle 110 \rangle$ LSV devices are discussed. This study clarifies that the anisotropic spin injection/detection efficiency should be considered for developing Si-

based spintronic devices.

2. Growth and device fabrication

First, we grew epitaxial CoFe/MgO layer as spin injector and detector on a phosphorous-doped ($n \sim 1.3 \times 10^{19}$ cm^{-3}) (001)-SOI ($\sim$ 61 nm) substrate. Note that a 1.1 nm-thick MgO layer was deposited by electron-beam evaporation at 200 °C on the Mg-terminated SOI layer [34]. During the growth, the crystalline MgO layer can be observed by reflection high-energy electron diffraction (RHEED) patterns, as shown in figures 1(a) and 1(b). Then, a 10-nm-thick CoFe layer was sputtered on the MgO surface under a base pressure better than 5.0 $\times$ 10^{-7} Pa. From the RHEED observation, good two-dimensional epitaxial growth can be confirmed, as shown in figures 1(c) and 1(d). Finally, a Ru cap layer (7 nm) was sputtered on top of it. The MgO and CoFe layers were epitaxially grown on (001)-SOI, where the (001)-textured MgO layer was grown on (001)-Si owing to an insertion of thin Mg layer into MgO/Si interface [35]. From the detailed characterizations, the CoFe(001)$\langle$100$\rangle$/MgO(001)$\langle$110$\rangle$/Si(001)$\langle$110$\rangle$ heterostructures were confirmed [35]. Figure 1(e) shows normalized field-dependent

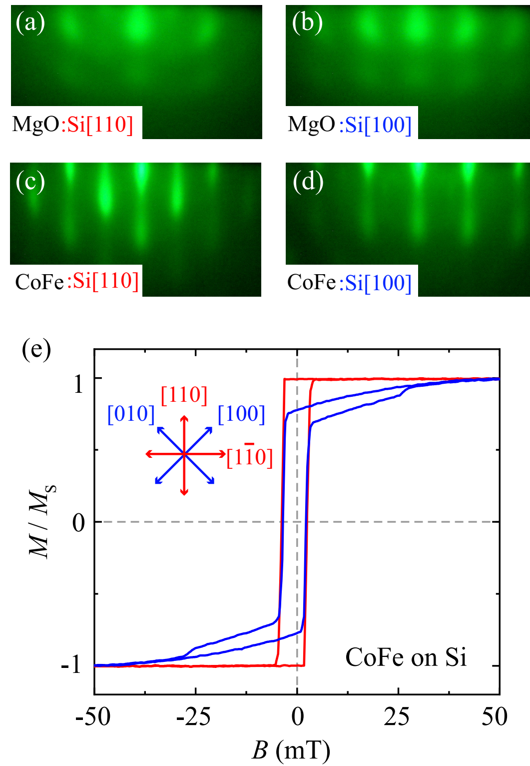

Figure 1. (Color online) *In-situ* RHEED patterns of the surfaces for MgO and CoFe epilayers observed along Si[110] [(a), (c)] and Si[100] [(b), (d)] directions. (e) Normalized field-dependent magnetization curves of epitaxially grown CoFe/MgO layer on (100)-SOI at room temperature. The inset shows in-plane crystallographic orientations of (100)-SOI.

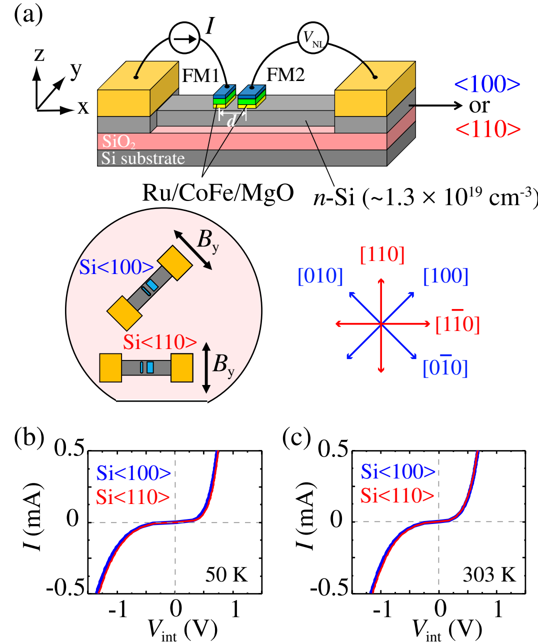

Figure 2. (Color online) (a) Schematic diagram of a lateral spin-valve (LSV) device with Si spin-transport channel along Si⟨100⟩ or Si⟨110⟩. Here the relationship among the crystal orientations, ⟨100⟩ or ⟨110⟩, the fabricated Si spin-transport channels, the applied field directions is shown. $I - V_{\rm int}$ characteristics for the CoFe-MgO/Si spin-injector interfaces at (b) 50 K and (c) room temperature (303 K).

magnetization curves measured along Si⟨100⟩ and Si⟨110⟩ at room temperature. It should be noted that weak magnetocrystalline anisotropy of epitaxial CoFe layer can be observed. Since the direction of Si⟨110⟩ is corresponding to that of CoFe⟨100⟩, we can confirm a magnetic easy axis for the measurement along Si⟨110⟩. On the other hand, the direction of Si⟨100⟩ is a magnetic hard axis, but there is the distribution of the magnetic anisotropies because of the presence of the two-step switching.

To explore the influence of the crystal orientation of the Si spin-transport channel, we designed two kinds of devices along ⟨100⟩ and ⟨110⟩, as shown in figure 2(a). Conventional processes with electron beam lithography and Ar ion milling were used to fabricate LSVs [20, 23–26]. The Ru/CoFe/MgO contacts were patterned into 2.0 × 5.0 μm^2 and 0.5 × 5.0 μm^2 in sizes, respectively, and the width of the Si spin-transport channel was 7.0 μm. As a result, the cross-sectional area of the n-Si layer was 0.305 μm^2. To estimate the spin diffusion length of the Si spin-transport channel, we fabricated LSV devices with various center-to-center distances (d) between CoFe/MgO contacts from 1.75, 2.25, 3.25, and 4.25 μm. Finally, Au/Ti ohmic pads were formed for all the contacts. Note that there is no difference in the size of the spin-injector contact between Si⟨100⟩ and Si⟨110⟩ LSVs [21]. Figures 2(b) and 2(c) show the $I - V_{\rm int}$ characteristics for CoFe-MgO/Si spin-injector interfaces at 50 K and room temperature (303 K), respectively, where $V_{\rm int}$ is the applied voltage to the CoFe-MgO/Si interfaces. These data were measured by the three-terminal configuration. Each interface clearly

shows tunneling conduction and the $I - V_{\rm int}$ behavior for both Si⟨100⟩ and Si⟨110⟩ LSV devices are almost the same irrespective of temperature, indicating the same interface condition at CoFe-MgO/Si heterostructure. These data means that the quality of the spin injector in both LSV devices is equivalent to explore the effect of the crystal orientation of the spin transport channel on the nonlocal spin transport. We also confirmed that the quality of the spin detector is also the same as well as the spin injector. Apart from them, the resistivity and Hall mobility ($\mu_{\rm Hall}$) of the Si spin-transport channel were evaluated from Hall-effect measurements for Si⟨100⟩ and Si⟨110⟩ Hall-bar devices.

3. Nonlocal spin transport

Figures 3(a) and 3(b) show four-terminal nonlocal magnetoresistance signals ($\Delta R_{\rm NL} = \Delta V_{\rm NL}/I$) for Si⟨100⟩ and Si⟨110⟩ LSV devices, respectively, at a bias current (I) of -0.5 mA at 50 K, where d in the LSVs was 1.75 μm. Here in-plane external magnetic fields ($B_{\rm y}$) were applied along the directions shown in figure 2(a) for each Si⟨100⟩ or Si⟨110⟩ LSV devices. First, we can see differences in the shape and magnitude of the signals between Si⟨100⟩ and Si⟨110⟩ LSV devices. These differences were always observed for more than ten LSV devices fabricated here. Also, we have already confirmed the reliable lateral spin transport detected by nonlocal-Hanle measurements in the same LSV devices, similar to the data in Ref. [20].

From the magnetization measurements of the epitaxial CoFe layer in figure 1(e), we have confirmed the presence of the magnetocrystalline easy axis along Si⟨110⟩ (CoFe⟨100⟩). Namely, as the direction of $B_{\rm y}$ (along Si⟨100⟩ ([100] or [010])) is switched from negative to positive, the magnetization reversal in the wider CoFe contact occurs but the magnetization direction is pinned along a certain direction between Si⟨110⟩ and the direction of $B_{\rm y}$ (Si⟨100⟩), as shown in figure 3(c)-1. With increasing $B_{\rm y}$, the magnetization rotation in the wider CoFe contact can be induced [figure 3(c)-2], leading to the antiparallel magnetization state. After further increase in $B_{\rm y}$, the magnetization of the narrower CoFe contact can switch toward the direction of $B_{\rm y}$, as shown in figure 3(c)-3, resulting in the parallel magnetization state. This feature can clearly be seen in the nonlocal magnetoresistance hysteresis loop for Si⟨100⟩ LSV device, as denoted by the number from 1 to 3 in figure 3(a).

On the other hand, for Si⟨110⟩ LSV devices, we can interpret that the magnetization reversal process of the CoFe contacts can occur just along Si⟨110⟩ parallel to the easy axis of the CoFe epilayer as the direction of $B_{\rm y}$ (along Si⟨110⟩ ([110] or [$1\bar{1}0$])) is switched from negative to positive. Since the effect of the shape anisotropy in the wider CoFe contact is not so large, the magnetization rotation in the wider CoFe contact from one easy axis to another one can be considered in low $B_{\rm y}$ region, as shown in figure 3(c)-4. In figure 3(b) the nonlocal signal is gradually changed from negative $B_{\rm y}$ to zero field. Then, as the magnetization direction of the wider CoFe contact is switched toward the direction of $B_{\rm y}$, the antiparallel magnetization state is formed, as shown in figures

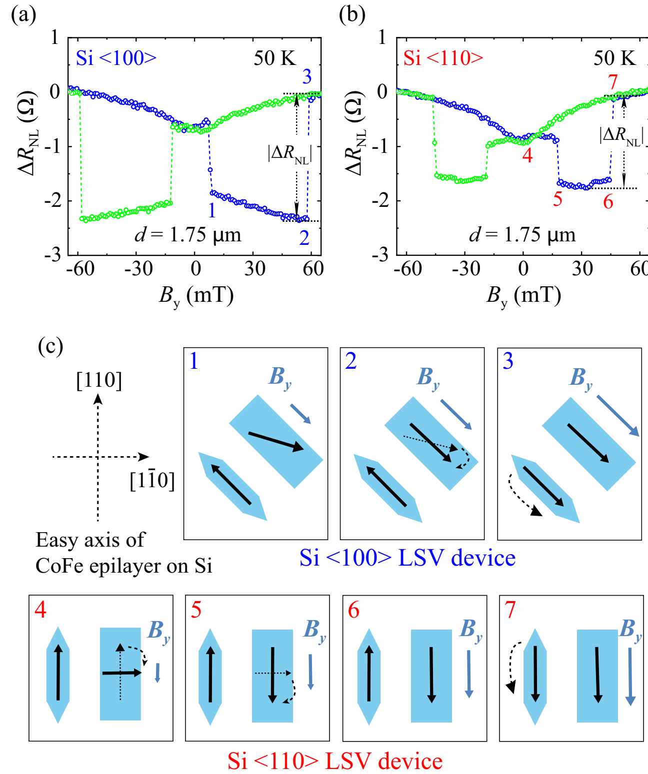

Figure 3. (Color online) Nonlocal magnetoresistance curves at 50 K for (a) Si⟨100⟩ and (b) Si⟨110⟩ LSVs. (c) Schematics of the magnetization states of the CoFe contacts under applying in-plane magnetic fields for Si⟨100⟩ and Si⟨110⟩ LSVs.

3(c)-5 and 3(c)-6. Finally, with increasing B_{y}, the parallel magnetization state can be formed, as shown in figure 3(c)-7, because of the magnetization reversal of the narrower CoFe contact. From these considerations, the hysteretic features observed in nonlocal magnetoresistance measurements can roughly be interpreted.

However, the difference in the magnitude of the magnetization switching fields between Si⟨100⟩ and Si⟨110⟩ LSV devices cannot be understood yet. Because these measurements were conducted within ± 100 mT, we can expect that the magnetization of the CoFe contacts was not to be fully saturated. Thus, to compare the magnetization reversal process of the CoFe contacts between Si⟨100⟩ and Si⟨110⟩ LSV devices, we probably should take into account the complicated domain-wall nucleation and propagation in the CoFe contacts fabricated epitaxially on Si. Although this feature is also under discussion, the complicated magnetic configuration may influence the presence of the broad change in the resistance at around zero-field. To discuss the magnitude of the nonlocal spin signlas, we focus on steep nonlocal magnetoresistance changes with the maximum value of ΔR_{NL}, as denoted in figures 3(a) and 3(b), when the magnetization state between the narrower and wider contacts is switched from anti-parallel to parallel at a higher B_{y}. Therefore, we hereafter define $|\Delta R_{\mathrm{NL}}|$ as a steep change in the value of ΔR_{NL} at a higher B_{y}, as shown in figures 3(a) and 3(b).

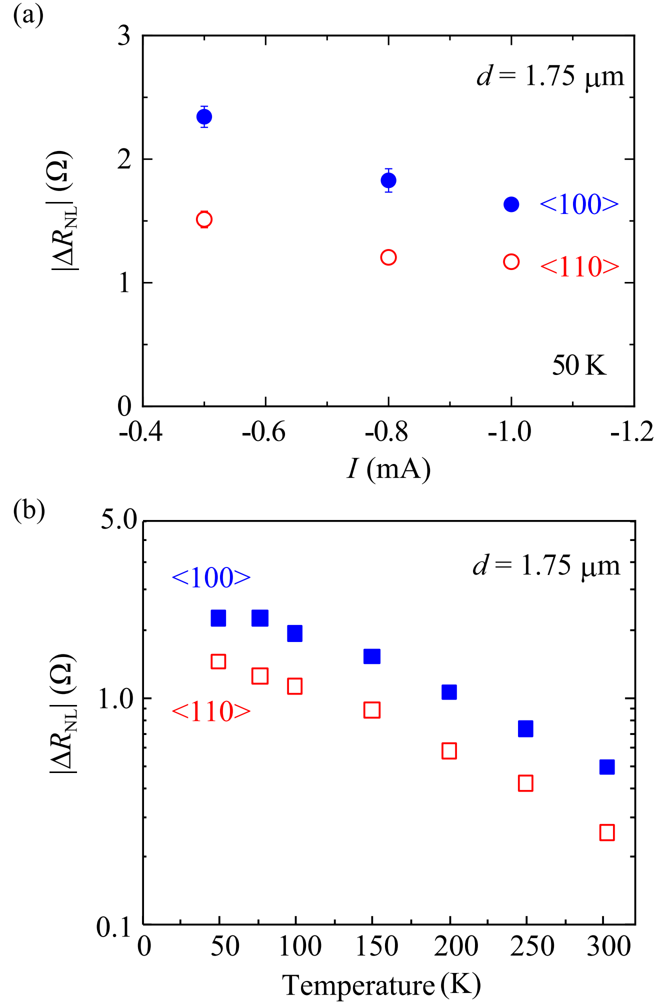

Figure 4. (Color online) (a) Bias current (I) dependence of ΔR_{NL} at 50 K and (b) temperature dependence of ΔR_{NL} for Si$\langle 100 \rangle$ and Si$\langle 110 \rangle$ LSVs.

In figure 4(a) we investigate bias current dependence of $|\Delta R_{\mathrm{NL}}|$ at 50 K by using LSV devices with $d = 1.75$ μm. Here the negative bias current ($I < 0$) means the condition of the spin injection from CoFe/MgO contacts into Si. The value of $|\Delta R_{\mathrm{NL}}|$ is slightly decreased with increasing negative I, similar to those reported in previous works. It should be noted that $|\Delta R_{\mathrm{NL}}|$ for the Si$\langle 100 \rangle$ LSV device is larger than that for the Si$\langle 110 \rangle$ LSV device in all the used I values. In this study, the observed difference in $|\Delta R_{\mathrm{NL}}|$ between Si$\langle 100 \rangle$ and Si$\langle 110 \rangle$ LSV devices does not depend on the value of I ($I <$ 0). As a bias current of -0.5 mA, we next compare the value of $|\Delta R_{\mathrm{NL}}|$ as a function of temperature, as shown in figure 4(b). From 50 K to 303 K, we can evidently see that $|\Delta R_{\mathrm{NL}}|$ for the Si$\langle 100 \rangle$ LSV device is larger although the value of $|\Delta R_{\mathrm{NL}}|$ is decreased with increasing external temperature. Thus, the difference in $|\Delta R_{\mathrm{NL}}|$ observed here might be intrinsic nature for Si-based LSV devices with crystallographic effect.

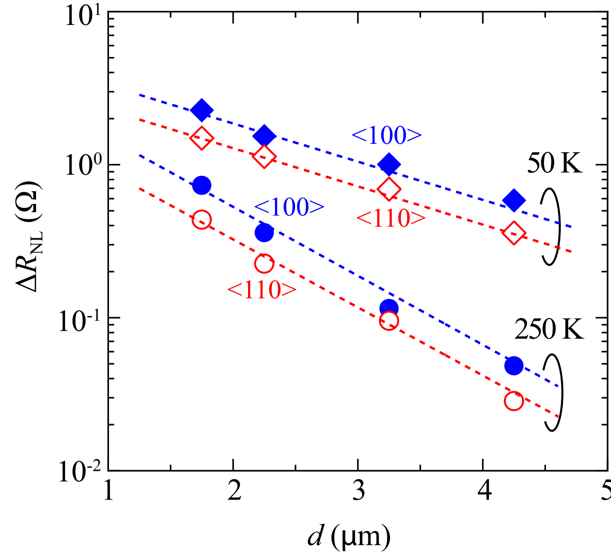

Figure 5. (Color online) d dependence of $|\Delta R_{\mathrm{NL}}|$ at 50 K and 250 K for Si⟨100⟩ and Si⟨110⟩ LSVs. The dashed lines show the results of fitting to Eq. (1).

4. Extraction of parameters

To understand the above phenomena, we measured d dependence of $|\Delta R_{\mathrm{NL}}|$ for both Si⟨100⟩ and Si⟨110⟩ LSV devices, as shown in figure 5. Here the one data plot in figure 5 means the average of the $|\Delta R_{\mathrm{NL}}|$ value obtained from five LSV devices. For both LSV devices, the value of $|\Delta R_{\mathrm{NL}}|$ is decreased with increasing d, indicating the exponential decay of $|\Delta R_{\mathrm{NL}}|$ from 50 K to 303 K. In general, $|\Delta R_{\mathrm{NL}}|$ in the LSVs with sufficiently large contact resistance can be expressed by the following equation: [36–39]

$$|\Delta R_{\mathrm{NL}}| = \frac{4|P_{\mathrm{inj}}||P_{\mathrm{det}}|r_{\mathrm{Si}}r_{\mathrm{b}}^2 \exp\left(-\frac{d}{\lambda_{\mathrm{Si}}}\right)}{S_{\mathrm{N}}\{(2r_{\mathrm{b}}+r_{\mathrm{Si}})^2 - r_{\mathrm{Si}}^2 \exp\left(-\frac{2d}{\lambda_{\mathrm{Si}}}\right)\}}, \quad (1)$$

where P_{inj} and P_{det} are spin polarizations of the electrons in Si created by the spin injector and detector, respectively, and $\sqrt{|P_{\mathrm{inj}}||P_{\mathrm{det}}|}$ generally means the spin injection/detection efficiency of the spin injector and detector contacts. r_{b} ($\sim$ 10 kΩ μm^2) and r_{Si} ($=$ 0.0054 Ω cm $\times\ \lambda_{\mathrm{Si}}$) are the spin resistances of the CoFe/MgO interface and the n-Si layer, respectively. λ_{Si} ($= \sqrt{D\tau_{\mathrm{Si}}}$, where D and τ_{Si} are the diffusion constant and the spin lifetime, respectively) is the spin diffusion length in Si, S_{N} ($=$ 0.305 μm^2) is the cross-sectional area of the Si spin transport layer. Using Eq. (1), we can fit the experimental data, as shown in figure 5, and extract λ_{Si} for both Si⟨100⟩ and Si⟨110⟩ spin-transport channels.

In figure 6 we display the temperature-dependent λ_{Si}, estimated from d-dependence data described above, for Si⟨100⟩ and Si⟨110⟩ LSV devices. From 50 K to 303 K, the value of λ_{Si} is decreased with increasing temperature, which can be interpreted in terms of the intervalley spin-flip scattering induced by the electron-phonon interactions [20,40].

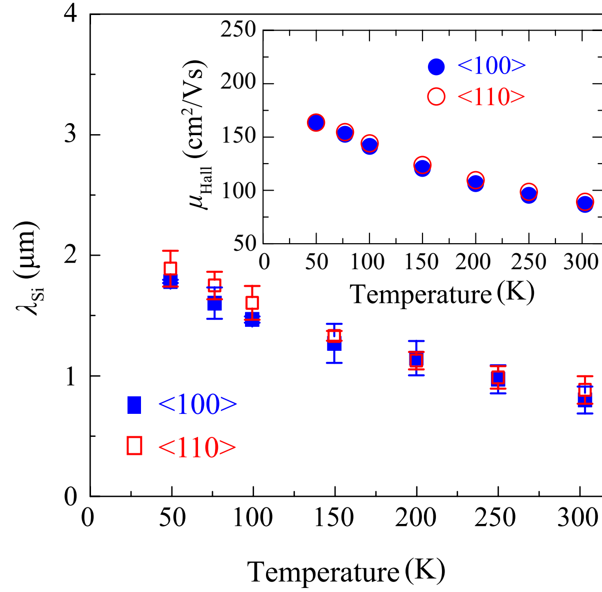

Figure 6. (Color online) Temperature dependence of λ_{Si}, estimated by d dependences of nonlocal spin signals at various temperatures, for Si$\langle 100\rangle$ and Si$\langle 110\rangle$ LSVs. The inset shows the temperature-dependent μ_{Hall}.

Note that the difference in the temperature dependence of λ_{Si} between Si$\langle 100\rangle$ and Si$\langle 110\rangle$ LSV devices is quite small in the measurement temperature range. Here we also measured μ_{Hall} in the inset of figure 6 and we confirmed that there is almost no difference in μ_{Hall} between Si$\langle 100\rangle$ and Si$\langle 110\rangle$.

When we use these data, the spin lifetime (τ_{Si}) can roughly be discussed. For example, by using the following relation, $\sqrt{D\tau_{Si}}$, where D values of 5.03 cm^2/s for Si$\langle 100\rangle$ (μ_{Hall} = 87.0 cm^2/Vs) and 5.17 cm^2/s for Si$\langle 110\rangle$ (μ_{Hall} = 89.5 cm^2/Vs) estimated from the Hall mobility [41], room-temperature τ_{Si} of 1.3 ns and 1.5 ns for Si$\langle 100\rangle$ and Si$\langle 110\rangle$, respectively, can be calculated. These τ_{Si} values were nearly consistent with those estimated from four-terminal nonlocal Hanle measurements. These tendencies were also confirmed at lower temperatures. From these experimental facts, we can judge that the difference in the spin relaxation between Si$\langle 100\rangle$ and Si$\langle 110\rangle$ is relatively small compared to other parameters.

On the other hand, the obtained $\sqrt{|P_{inj}||P_{det}|}$ value of ~ 0.16 for the Si$\langle 100\rangle$ LSV device is valuably larger than that ($\sqrt{|P_{inj}||P_{det}|} \sim 0.11$) for the Si$\langle 110\rangle$ LSV device even at room temperature. Figure 7 shows the temperature dependence of $\sqrt{|P_{inj}||P_{det}|}$ for both Si$\langle 100\rangle$ and Si$\langle 110\rangle$ LSV devices. Although the values of $\sqrt{|P_{inj}||P_{det}|}$ are decreased with increasing temperature for both LSV devices, the $\sqrt{|P_{inj}||P_{det}|}$ value for the Si$\langle 100\rangle$ LSV device is always larger than that for Si$\langle 110\rangle$ LSV device. Thus, we can expect that the spin injection/detection efficiency for Si$\langle 100\rangle$ LSV devices is intrinsically large compared to that for Si$\langle 110\rangle$ LSV devices.

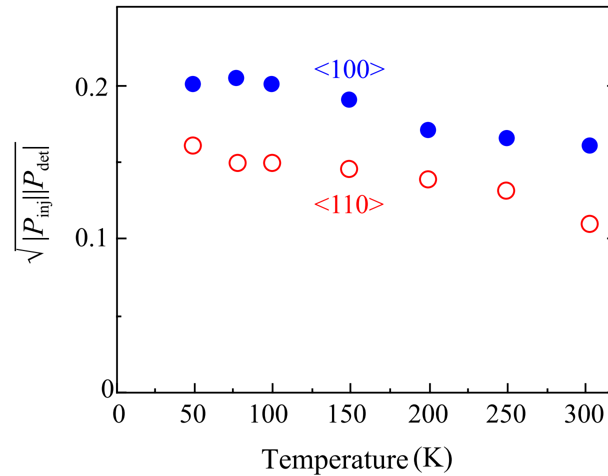

Figure 7. (Color online) Temperature dependence of the spin injection/detection efficiency ($\sqrt{|P_{\rm inj}||P_{\rm det}|}$) for Si$\langle 100\rangle$ and Si$\langle 110\rangle$ LSVs.

5. Discussion

We discuss possible origins of the difference in the spin injection/detection efficiency, $\sqrt{|P_{\rm inj}||P_{\rm det}|}$, between Si$\langle 100\rangle$ and Si$\langle 110\rangle$ LSV devices. First, the g-factor anisotropy in Si is negligibly small compared to that in Ge because of the weak spin orbit interaction [43, 44]. This fact means that, unlike Ge, we cannot see the change in the spin transport data only by changing the direction of the applied magnetic fields [29]. Actually, we performed oblique Hanle measurements for a Si LSV and confirmed the negligible change in the Hanle curves by changing the applied field directions (not shown here).

Next, we should consider the presence of the tunneling anisotropic spin polarization on, which was discovered in (Ga,Mn)As/GaAs LSV devices [31]. In general, the tunneling anisotropic spin polarization is due to the magnetization direction of the ferromagnetic contacts relative to the crystal orientation of semiconductors [31–33]. Although the origin of the presence of the tunneling anisotropic spin polarization has not been discussed in detail [31–33], the magnetization direction of ferromagnetic contacts relative to the crystal axis in between Si$\langle 100\rangle$ and Si$\langle 110\rangle$ LSV devices should be considered. We infer that the tunneling anisotropic spin polarization is one of the possible origins of the crystal orientation effect on the spin injection/detection efficiency in Si LSV devices.

Finally, as another possible origin, we discuss the crystallographic effect of the conduction band valleys in Si. Figure 8(c) illustrates the conduction-band valley positions in the **k**-space in Si; six valleys are located close to the X point along $\langle 100\rangle$. Using a full-orbital tight-binding model, similar to those in previous reports [45, 46], we roughly calculate the spin polarization of the tunnel current, spin-resolved tunnel current $I_{\uparrow}$ and $I_{\downarrow}$, for a ferromagnet (FM)/MgO/Si junction. Here the tunnel junction used in this calculation is a CoFe-MgO(0.5 nm)/Si stacked structure for simplicity, and the

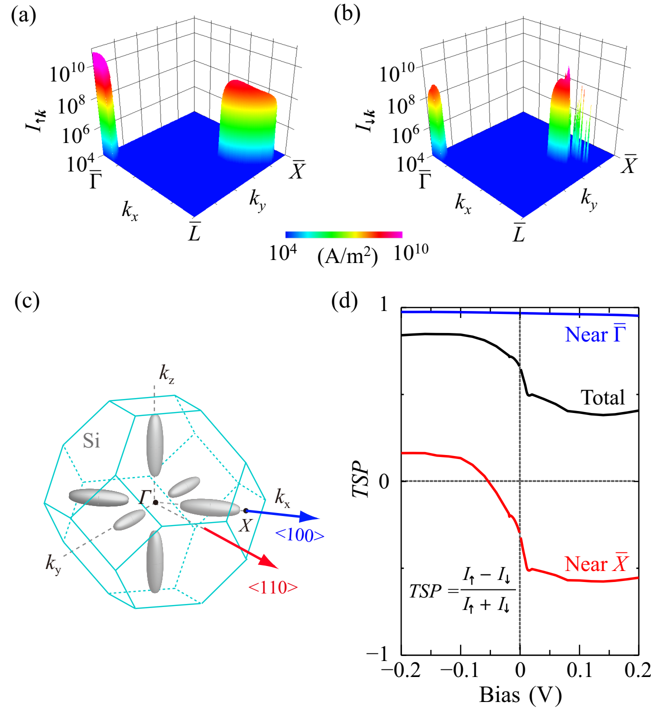

Figure 8. (Color online) Momentum-resolved tunnel current I for (a) spin-up (↑) and (b) spin-down (↓). (c) Schematic diagram of Brillouin zone of bulk Si. (d) Calculated tunneling spin polarization (TSP) as a function of bias voltage.

electronic structure of CoFe is given by shifting the up-spin and down-spin Fe bands [47] to −1.12 eV and −0.74 eV, respectively. The electronic structure of Si is given by Boykin's parameters [48]. The tight-binding parameter of MgO and the hopping matrix of each interface are determined by the Harrison method [49]. Figures 8(a) and 8(b) show the momentum-resolved I for spin-up (↑) and spin-down (↓), respectively, where the barrier height, barrier thickness, and bias voltage are 1.0 eV, 0.5 nm, and −0.1 V [50], respectively, and the magnetization of the CoFe layer is aligned long $\langle 100\rangle$ because of the magnetocrystalline anisotropy. In both spin states, not only the component of I around the Γ point but also that around the X point can be seen evidently because the six conduction-band valleys are located close to the X point along $\langle 100\rangle$ in the **k**-space in Si, as shown in figure 8(c). This feature means that the tunneling spin polarization (TSP) in the FM/MgO/Si junctions can be affected by the X-point component in the electrical spin injection and detection. Figure 8(d) presents the calculated TSP as a function of bias voltage applied to the CoFe/MgO/Si junction. In all the calculated bias conditions, the magnitude of TSP is governed by the Γ-point component but the bias-dependent behavior is evidently affected by the X-point one. From these calculations, we can expect that the conduction band valleys in Si contribute to the anisotropy of the electrical spin injection and detection through the FM/MgO/Si junctions.

The calculated data in figures 8 depended strongly on the barrier height and barrier thickness of the MgO tunnel barrier. When the barrier height and barrier thickness are

higher and thicker than 1.0 eV and 0.5 nm, respectively, the magnitude of TSP from the X-point component was markedly suppressed because of the enhancement in the Γ-point component. As a result, the X-point component in the electrical spin injection and detection was strongly limited. Thus, the influence of the conduction band valleys in Si on the spin injection/detection efficiency is probably limited for LSVs with a thin MgO tunnel barrier. On the other hand, the tunneling anisotropic spin polarization described before was observed in other junction conditions in Si devices [32, 33]. Although the precise origin is still unclear, we infer that possible origins of the difference in the spin injection/detection efficiency between Si⟨100⟩ and Si⟨110⟩ LSV devices are the tunneling anisotropic spin polarization due to the magnetization direction of the ferromagnetic contacts relative to the crystal orientation of semiconductors [31–33] or the influence of the conduction band valleys in Si, discussed in figures 8. For Si-based spintronic applications, it is important to consider the crystal orientation effect described in this paper.

6. Conclusion

We have investigated the crystal orientation effect on pure spin current transport in Si-based LSV devices with epitaxially grown CoFe/MgO tunnel contacts. When we compared nonlocal spin signals between LSV devices along ⟨100⟩ (Si⟨100⟩ and ⟨110⟩ (Si⟨110⟩), the magnitude of the spin signals for Si⟨100⟩ LSV devices was always larger than that for Si⟨110⟩ LSV devices. From the analyses based on the one-dimensional spin diffusion model, we judged that the spin injection/detection efficiency in Si⟨100⟩ LSVs is evidently larger than that in Si⟨110⟩ ones. Possible origins were discussed on the basis of the tunneling anisotropic spin polarization shown in Ref. [31–33] or the influence of the conduction band valleys in Si. This study clarifies that it is important for Si-based spintronic applications to consider the crystal orientation effect.

Acknowledgments

M.I and K.H acknowledge Dr. H. Sugiyama of Toshiba Corporation for useful discussion about the pure spin current transport in Si and the magnetocrystalline anisotropy of the CoFe layer on MgO/(001)SOI, respectively. This work was partly supported by a Grant-in-Aid for Scientific Research (A) (No. 16H02333) from the Japan Society for the Promotion of Science (JSPS), and a Grant-in-Aid for Scientific Research on Innovative Areas "Nano Spin Conversion Science" (No. 26103003) from the Ministry of Education, Culture, Sports, Science, and Technology (MEXT).

References

[1] Žutić I, Fabian J and Sarma S D 2004 *Rev. Mod. Phys.* **76** 323
[2] Yuasa S and Djayaprawira D D 2007 *J. Phys. D: Appl. Phys.* **40** R337
[3] Taniyama T, Wada E, Itoh M and Yamaguchi M 2011 *NPG Asia Mater.* **3** 65

[4] Hirohata A and Takanashi K 2014 *J. Phys. D: Appl. Phys.* **47** 193001
[5] Tanaka M and Sugahara S 2007 *IEEE Trans. Electron Devices* **54** 961
[6] Dery H, Dalal P, Cywiński Ł and Sham L J 2007 *Nature (London)* **447** 573
[7] Saito Y, Marukame T, Inokuchi T, Ishikawa M, Sugiyama H and Tanamoto T 2011 *Thin Solid Films* **519** 8266; Saito Y, Inokuchi T, Ishikawa M, Sugiyama H, Marukame T and Tanamoto T 2011 *J. Electrochem. Soc.* **158** H1068
[8] Manipatruni S, Nikonov D E and Young Ian A 2018 *Nat. Phys.* **14** 338
[9] Lou X, Adelmann C, Crooker S A, Garlid E S, Zhang J, Reddy K S M, Flexner S D, Palmstrøm C J and Crowell P A 2007 *Nat. Phys.* **3** 197
[10] Ciorga M, Einwanger A, Wurstbauer U, Schuh D, Wegscheider W and Weiss D 2009 *Phys. Rev. B* **79** 165321
[11] Salis G, Fuhrer A, Schlittler R R, Gross L and Alvarado S F 2010 *Phys. Rev. B* **81** 205323
[12] Bruski P, Erwin S C, Herfort J, Tahraoui A and Ramsteiner M 2014 *Phys. Rev. B* **90** 245150
[13] Choi W Y, Kim H-j, Chang J, Han S H, Koo H C and Johnson M 2015 *Nat. Nanotechnol.* **10** 666
[14] Uemura T, Akiho T, Ebina Y and Yamamoto M 2015 *Phys. Rev. B* **91** 140410(R)
[15] Peterson T A, Patel S J, Geppert C C, Christie K D, Rath A, Pennachio D, Flatté M E, Voyles P M, Palmstrøm C J and Crowell P A 2016 *Phys. Rev. B* **94** 235309
[16] van't Erve O M J, Hanbicki A T, Holub M, Li C H, Awo-Affouda C, Thompson P E and Jonker B T 2007 *Appl. Phys. Lett.* **91** 212109
[17] Sasaki T, Oikawa T, Suzuki T, Shiraishi M, Suzuki Y and Noguchi K 2010 *Appl. Phys. Lett.* **96** 122101
[18] Suzuki T, Sasaki T, Oikawa T, Shiraishi M, Suzuki Y and Noguchi K 2011 *Appl. Phys. Express* **4** 023003
[19] Saito Y, Ishikawa M, Inokuchi T, Sugiyama H, Tanamoto T, Hamaya K and Tezuka N 2012 *IEEE Trans. Magn.* **48** 2739
[20] Ishikawa M, Oka T, Fujita Y, Sugiyama H, Saito Y and Hamaya K 2017 *Phys. Rev. B* **95** 115302
[21] Spiesser A, Saito H, Fujita Y, Yamada S, Hamaya K, Yuasa S and Jansen R 2017 *Phys. Rev. Appl.* **8** 064023
[22] Zhou Y, Han W, Chang L-T, Xiu F, Wang M, Oehme M, Fischer I A, Schulze J, Kawakami R K and Wang K L 2011 *Phys. Rev. B* **84** 125323
[23] Fujita Y, Yamada M, Yamada S, Kanashima T, Sawano K and Hamaya K 2016 *Phys. Rev. B* **94** 245302
[24] Yamada M, Fujita Y, Tsukahara M, Yamada S, Sawano K and Hamaya K 2017 *Phys. Rev. B* **95** 161304(R)
[25] Fujita Y, Yamada M, Tsukahara M, Oka T, Yamada S, Kanashima T, Sawano K and Hamaya K 2017 *Phys. Rev. Appl.* **8** 014007
[26] Yamada M, Tsukahara M, Fujita Y, Naito T, Yamada S, Sawano K and Hamaya K 2017 *Appl. Phys. Express* **10** 093001
[27] Rortais F, Vergnaud C, Marty A, Vila L, Attané J-P, Widiez J, Zucchetti C, Bottegoni F, Jaffrès H, George J-M and Jamet M 2017 *Appl. Phys. Lett.* **111** 182401
[28] Hamaya K, Fujita Y, Yamada M, Kawano M, Yamada S, and Sawano K 2018 *J. Phys. D: Appl. Phys.* **51** 393001
[29] Li P, Li J, Qing L, Dery H and Appelbaum I 2013 *Phys. Rev. Lett.* **111** 257204
[30] Park T-E, Park Y H, Lee J-M, Kim S W, Park H G, Min B-C, Kim H-j, Koo H C, Choi H-j, Han S H, Johnson M and Chang J 2017 *Nat. Comm.* **8** 15722
[31] Einwanger A, Ciorga M, Wurstbauer U, Schuh D, Wegscheider W and Weiss D 2009 *Appl. Phys. Lett.* **95** 152101
[32] Sharma S, Dash S P, Saito H, Yuasa S, van Wees B J and Jansen R 2012 *Phys. Rev. B* **86** 165308
[33] Sharma S, Spiesser A, Saito H, Yuasa S, van Wees B J and Jansen R 2013 *Phys. Rev. B* **87** 085307
[34] Ishikawa M, Sugiyama H, Inokuchi T, Hamaya K and Saito Y 2015 *Appl. Phys. Lett.* **107** 092402
[35] Saito Y, Inokuchi T, Ishikawa M, Ajay T and Sugiyama H 2017 *AIP Adv.* **7** 055937

[36] Saito Y, Ishikawa M, Sugiyama H, Inokuchi T, Hamaya K and Tezuka N 2015 *J. Appl. Phys.* **117** 17C707

[37] Takahashi S and Maekawa S 2003 *Phys. Rev. B* **67** 052409

[38] Fert A and Jaffrès H 2001 *Phys. Rev. B* **64** 184420

[39] Jaffrès H, George J-M and Fert A 2010 *Phys. Rev. B* **82** 140408(R)

[40] Song Y and Dery H 2012 *Phys. Rev. B* **86** 085201

[41] Flatté M E and Byers J M 2000 *Phys. Rev. Lett.* **84** 4220

[42] Jemeda F J, Heersche H B, Filip A T, Baselmans J J A and van Wees B J 2002 *Nature* **416** 713

[43] Wilson D K and Feher G 1961 *Phys. Rev.* **124** 1068

[44] Giorgioni A, Paleari S, Cecchi S, Vitiello E, Grilli E, Isella G, Jantsch W, Fanciulli M and Pezzoli F 2016 *Nat. Comm.* **7** 13886

[45] Honda S, Itoh H, Inoue J, Kurebayashi H, Trypiniotis T, Barnes C H W, Hirohata A and Bland J A C 2008 *Phys. Rev. B* **78** 245316

[46] Honda S, Itoh H and Inoue J 2010 *J. Phys. D: Appl. Phys.* **43** 135002

[47] Papaconstantopoulos D A 1986 *Handbook of the Band Structure of Elemental Solids* Plenum, New York

[48] Boykin T B, Klimeck G, and Oyafuso F 2004 *Phys. Rev. B* **69** 115201

[49] Harrison W 1980 *Electronic Structure and the Properties of Solids* Freeman, San Francisco

[50] The value of the barrier height (1.0 eV) is reasonable for our previous report: Saito Y, Ishikawa M, Sugiyama H, Inokuchi T, Hamaya K and Tezuka N 2015 *J. Appl. Phys.* **117** 17C707. Although the value of the barrier width (0.5 nm) is thinner than that of the used MgO thickness (1.1 nm), it is also reasonable because the quality of the MgO layer is not perfect in experiments.